

PdGa Alloying-Dealloying Processes under Reducing and CO₂ Hydrogenation Reaction Conditions from Metadynamics Simulations

Julian F. Baumgärtner,^{†,||} Andreas Müller,^{†,||} Scott R. Docherty,^{†,||} Aleix Comas-Vives,^{‡,§} Pierre-Adrien Payard,^{*,||,†} and Christophe Copéret^{*,†}

[†]Department of Chemistry and Applied Biosciences, ETH Zurich, Zurich, Switzerland

[‡]Departament de Química, Universitat Autònoma de Barcelona, 08193 Cerdanyola del Vallès, Catalonia, Spain

[§]Institute of Materials Chemistry, TU Wien, 1060 Vienna, Austria.

^{||}Université de Lyon, Université Claude Bernard Lyon I, CNRS, INSA, CPE, UMR 5246, ICBMS, 1 rue Victor Grignard, F-69622 Villeurbanne cedex, France

KEYWORDS. *Nanoparticle, Metadynamics, Ab-initio Molecular Dynamics, CO₂ Hydrogenation, Surface Organometallic Chemistry*

Silica-supported PdGa nanoparticles (NPs) prepared *via* Surface Organometallic Chemistry are selective catalysts for the hydrogenation of CO₂ to methanol. However, despite their notable catalytic performances, that exceed the corresponding Cu-based systems, little is understood regarding the local structure of the PdGa NPs, their adsorption properties, and their behaviour under CO₂ hydrogenation reaction conditions, making the development of structure–activity relationships challenging. Here, we use *ab-initio* Molecular Dynamics and Metadynamics at the density-functional theory level combined with *in-situ* X-ray absorption spectroscopy to explore the structures and the dynamics of the alloyed PdGa NPs under various conditions. We look in particular at the impact of the SiO₂ surface and adsorbates (H*, CO*, O*), expected under CO₂ hydrogenation conditions, onto the structure of the NPs. Overall, addition of Ga to Pd generates alloyed PdGa NP with isolated Pd sites at the surface. This structural change decreases the amount of adsorbed hydrogen or CO on the NPs and changes the dominant binding mode of the adsorbates to the metal, from mainly bridging to terminal CO and from mainly internal hydrides to terminal and μ_2 -bridging hydrides. Under more oxidizing conditions, akin to CO₂ hydrogenation for PdGa NPs, Ga is partially oxidised, forming a GaO_x layer on the surface of the NP, with a partially dealloyed PdGa core, that retains some isolated Pd sites at the surface. Overall, these bimetallic NPs show high structural dynamics and a variable extent of alloying in the presence of different adsorbates relevant for CO₂ hydrogenation.

Introduction

Supported metal nanoparticles (NPs) constitute one of the largest classes of catalysts, covering a broad range of applications, from selective hydrogenation to reforming and hydrocracking technologies.^{1–4} Among them, bimetallic NPs, composed of two transition metals or a combination of a transition metal and a main group element including metalloid, frequently display improved catalytic performances (activity, selectivity and/or stability) due to synergistic effects between the two elements,

hence their broad interest in both academia and industry.⁵⁻¹⁰ These supported bimetallic catalysts are inherently complex, involving particles of various sizes, compositions, and interfaces, leading to multiple structurally distinct sites, including alloys. Moreover, the chemical state of the active catalyst can respond dynamically to the composition and individual partial pressures of reactants and products, i.e. their chemical potentials.¹¹⁻¹⁴ This complexity poses a significant challenge for elucidating the distribution and nature of active sites, even when using advanced *in situ/operando* spectroscopic techniques and state-of-the-art computational modelling.¹⁵

Notably, bimetallic NPs show outstanding performances in the selective hydrogenation of CO₂ to methanol. This process is a crucial step for the so-called methanol economy, where green methanol is proposed as both an energy carrier and green feedstock in the chemical industry.¹⁶⁻²⁰ Despite years of research in this key technology, the reaction mechanism remains unclear; multiple active sites/states have been proposed across bimetallic systems, that include interface sites, surface alloys,^{21,22} active site defects,²³ and overlayers.^{24,25}

In that context, Surface Organometallic Chemistry (SOMC), in combination with thermolytic molecular precursors, has emerged as a powerful tool for interrogating the active structure of supported heterogeneous catalysts by generating tailored materials containing small, size-homogeneous (bimetallic) NPs with control of interfaces and composition, in the absence of bulk metal/oxide.²⁶⁻³² This approach has been successfully applied to various reactions, particularly CO₂ hydrogenation to methanol,³³⁻³⁵ propane dehydrogenation,^{36,37} and reforming.³⁸ For CO₂ hydrogenation catalysts, the most notable examples are silica-supported CuGa, CuZn, and PdGa NPs, which display a distinct reactivity compared to their monometallic counterparts.^{22,34,35,39-41} Notably, the two metals form an alloy in the as-prepared catalysts after H₂ treatment, as shown by X-ray absorption spectroscopy (XAS). Under CO₂ hydrogenation conditions, the alloyed Ga/Zn is partially reoxidised, while Cu or Pd remains metallic. Among these systems, the silica-supported PdGa catalysts, consisting of relatively small NPs (1.6 nm) supported on a Ga(III)-doped silica, are particularly interesting because of their significantly higher intrinsic methanol formation rate compared to the Cu equivalent. Apart from the dynamic alloying-dealloying, the PdGa alloy shows distinct adsorption properties towards H₂ and CO compared to the monometallic system, Pd@SiO₂. Furthermore, the distribution of CO species is greatly affected by the presence of Ga, as shown by infrared (IR) spectroscopy. These observations raise questions regarding i) the structure of the alloy at a single particle level (distribution of Ga in Pd), ii) the influence of the support on such structures, iii) how alloying affects the adsorption properties of probe molecules such as H₂ and CO and, iv) how such alloys structurally evolve under CO₂ hydrogenation conditions which correspond to rather oxidising conditions compared to CO hydrogenation.^{14,40}

In that context, computational modelling confronted with experimental data can help to answer these questions. While periodic calculations on slab models are usually used for modelling supported nanoparticles, they are less adequate to describe small particles (< 2-3 nm), for which the total number of atoms in the particle is relatively small. In contrast, the nanoparticle/support interfacial contributions to the stabilization of the system are large. Modelling is further complicated by possible dynamic processes under reaction conditions, e.g. interaction with adsorbates.²⁵

Recent efforts from our group have shown that *ab initio* molecular dynamics (AIMD),⁴² in combination with Metadynamics (MTD)⁴³⁻⁴⁷ confronted with experimental data, can be a powerful tool to explore plausible structures and dynamic processes in supported metal alloys in propane dehydrogenation.^{48,49} Here, we use this approach to examine the structure of PdGa NPs supported on silica under various reactive environments. We first refine the structure of PdGa NPs and study the influence of the SiO₂ support on their structure, before addressing the reactivity of PdGa NPs under different reactive gas atmospheres – H₂, CO, and the oxidizing conditions corresponding to CO₂ hydrogenation. Finally, we discuss the broader implications of these results on the structure, reactivity, and stability of bimetallic NPs.

Experimental Systems and Structure of Pristine PdGa Nanoparticles

To gain insights into the distribution of Ga and Pd in the particles, we use AIMD/MTD to refine the structure of the as-synthesised catalyst by first exploring the most stable structures of PdGa NPs. We first investigate a PdGa NP containing a total of 38 atoms, in the absence of the support, with Pd/Ga ratio of ca. 1:1 (0.8 nm, 18 Pd atoms, 20 Ga atoms, compare Figure 1 b) (i)), close to the experimental particle size and composition.³⁹ The Pd and Ga coordination numbers (CN_{Pd-Pd} , CN_{Pd-Ga} , and CN_{Ga-Ga} , s. computational methods for definition) were used as collective variables (CVs) to explore the free energy surface (FES) for all MTD simulations. These CVs were chosen since they allow us to distinguish various alloyed and segregated structures possible for the NPs.

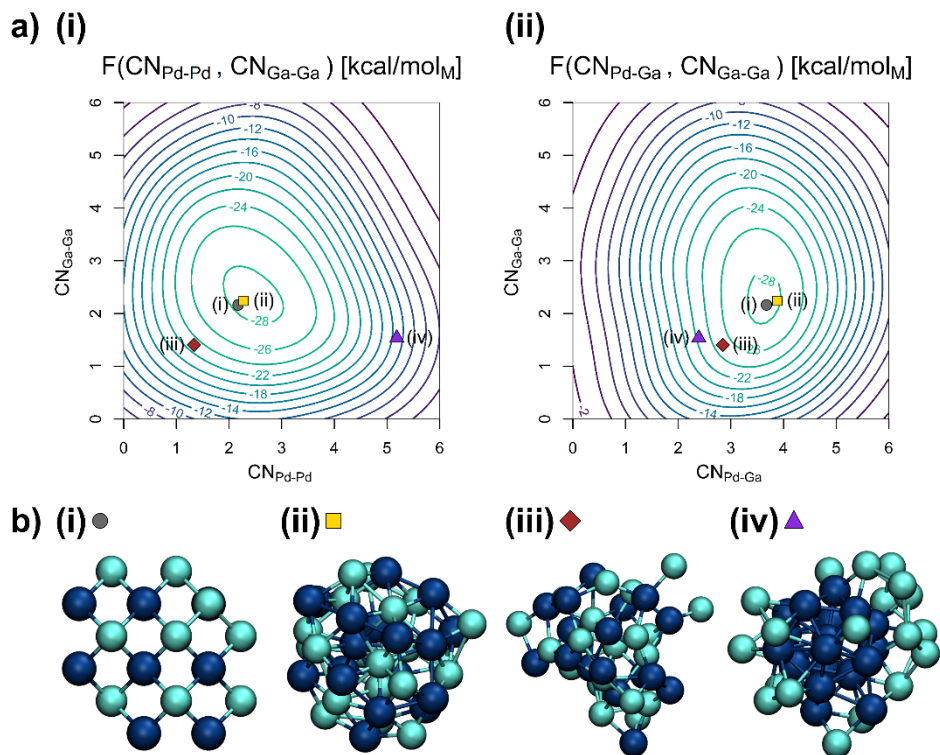


Figure 1: a) Free energy surfaces (FES) of the Pd₁₈Ga₂₀ NP in vacuum in kcal/mol_M based on (i) CN_{Pd-Pd} and CN_{Ga-Ga} as well as (ii) CN_{Pd-Ga} and CN_{Ga-Ga} with the minimum located at $CN_{Pd-Pd} = 2.5$, $CN_{Pd-Ga} = 3.7$ and $CN_{Ga-Ga} = 2.3$. b) Structures of the Pd₁₈Ga₂₀ NP in vacuum visited during the trajectory including (i) starting guess, (ii) structure closest to the free energy minimum, (iii) statistically mixed structure and (iv) structure with a Pd-core. Pd: dark blue; Ga: brighter blue. See the SI for in-depth treatment of the trajectory (Figures S6-S11).

The conformational space of the NP was explored by MTD (Figure S6). Both segregated and alloyed structures are sampled over the course of the simulation, as evidenced by the selected structure snippets (Figures 1 b) (ii) – (iv)). CN_{Pd-Pd} varies rapidly between 0.8 and 5.2, whereas CN_{Pd-Ga} varies between 1.8 and 4.2, and CN_{Ga-Ga} varies between 0.7 and 4.8 (Figure S6). The free energy minimum corresponds to an alloyed structure located at $CN_{Pd-Pd} = 2.5$, $CN_{Pd-Ga} = 3.7$, and $CN_{Ga-Ga} = 2.3$. This structure features mainly isolated Pd sites surrounded by an average of 4 Ga atoms, similar to the crystalline bulk model (Figure 1 b) (i)), indicating that segregation of the two metals, either as a Janus particle or a core-shell structure, is disfavoured energetically. No crystalline structures are observed, likely due to increased particle dynamics associated with the small particle size.^{50–52}

The shape of the FES in Figure 1 a) indicates that CN_{Pd-Ga} is not easily changed while both CN_{Pd-Pd} and CN_{Ga-Ga} have more shallow minima in the FES. The shallow FES for some of the CVs allows efficient exploration of different structures, including core-shell structures with a Ga-enriched shell (Figure 1 b) (iv)). Interestingly, only one distinct minimum was found on the FES, which indicates that the particles are distributed around the minima rather than having different phases. Thus, the structure of the small PdGa NP can be described as highly dynamic and inherently disordered.

Alloying is likely driven by two factors. First, alloying increases the mixing entropy. Nonetheless, if the mixing entropy was the only driving force, a statistical alloy with Cowley Short Range Order Parameters of $\alpha_{Pd-Ga} = \alpha_{Ga-Pd} = 0$ (Figure 1 b) (iii)) would be obtained (see SI for an in-depth discussion of the Cowley Short Range Order Parameter⁵³⁻⁵⁶). Yet, $\alpha_{Ga-Pd} = -0.24$ ($\alpha_{Pd-Ga} = -0.14$) are significantly smaller than 0, indicating that there must also be an additional enthalpic factor that disfavors a purely statistical distribution. Previous computational studies found that among the three bond combinations, Pd-Ga bonds are the strongest and significantly shorter than individual monometallic bonds.⁵⁷ Hence, short-range Pd-Ga interactions are maximized while weaker Ga-Ga and Pd-Pd bonds are broken. The strong preference for Pd-Ga bonds is confirmed by the CN_{Pd-Ga} of around 4. In contrast, Pd-Pd and Ga-Ga bonds are readily interconverted without changing the overall free energy of the structure significantly due to their low formation enthalpies. Such weaker bonds also partially account for the higher fluxionality of PdGa NPs compared to pure Pd. Overall, PdGa alloying implies that Pd atoms are diluted in the structure compared to pure Pd NPs, an observation that is overall consistent with EXAFS fits (*vide infra*), suggesting that Pd atoms are well-dispersed at the surface, as well as in the bulk.

Impact of SiO₂-surface on the structure of PdGa

Previous analyses of the Pd K-edge Extended X-Ray Absorption Fine Structure (EXAFS) of pristine PdGa@SiO₂ gives path degeneracies for Pd-Pd and Pd-Ga first shell scattering of 3.1 ± 0.9 and 2.8 ± 0.9 , respectively.³⁹ Notably, the Pd-Pd path degeneracy is significantly lower than that of the monometallic analogue, Pd@SiO₂ ($CN_{Pd-Pd} = 8.1 \pm 0.4$), which is to be expected when Pd is diluted with Ga. Furthermore, analysis of the Ga K-edge X-Ray Absorption Near Edge Spectroscopy (XANES) suggests that predominantly reduced Ga is present, alloyed with Pd, while some Ga(III) is retained.

The presence of oxidised Ga in the as-prepared supported PdGa NPs cannot be accounted for by a model without a silica support. We thus decided to explore the influence of the support onto the PdGa NPs, since such support effects can influence the coordination environment of the elements in the particle, as recently shown for PtGa and PtMn NPs supported on dehydroxylated silica.^{48,49} Thus, we took a pre-optimised structure of a PdGa NP and placed it onto a model surface of dehydroxylated amorphous silica with a Ga(III) single site, used to synthesise the PdGa NPs.^{39,58} CN_{Pd-O} and CN_{Ga-O} were added as CVs to model interactions between the PdGa NP and the SiO₂ surface (Figure S12).

The FES (Figure S20) indicates that the minimum free energy structure deviates from the PdGa NP in vacuum, with CN_{Pd-Pd} decreasing from 2.5 to 1.8, CN_{Pd-Ga} decreasing from 3.6 to 3.0, and CN_{Ga-Ga} increasing from 2.3 to 2.6. While this demonstrates a clear interaction between NP and SiO₂ surface, CN_{Pd-O} and CN_{Ga-O} are close to 0, indicating that no covalent bonds are formed between the support and the NP. As a result, the overall structure of the bimetallic NP supported on the SiO₂ surface does not change significantly.

Thus, surface interactions cannot account for the oxidised Ga retained in the precatalyst after H₂ treatment. Instead, the observed oxidised Ga is most likely due to retention of some tetracoordinated Ga-sites at the catalyst surface, which were not accounted for in the simulation.³⁹

Hence, the Ga K-edge EXAFS for pristine PdGa@SiO₂ was fitted as well (Figures S1-S4, Tables S1-S3). A Ga-Pd path degeneracy of 0.7 ± 0.2 ($R_{Ga-Pd} = 2.49 \pm 0.01$ Å) and a Ga-O path degeneracy of 2.9 ± 0.4 ($R_{Ga-O} = 1.84 \pm 0.01$ Å) was obtained. The lower average Ga-Pd path degeneracy from the Ga K-edge compared to the Pd-Ga path degeneracy from the Pd K-edge most likely

arises from the fact that a significant proportion of Ga(III) silicate is retained, even after H₂ treatment. Comparing the unsupported PdGa NPs with the SiO₂-supported system shows that qualitative features like alloying and Pd site isolation are successfully reproduced in both models. As a first approximation, the support can be assumed mostly innocent. Therefore, subsequent modelling utilizes the unsupported PdGa NP model.

Structure of COs on PdGa-Catalysts

Next, we modelled both PdGa and Pd NPs with adsorbed CO* in order to better understand the significant differences between the adsorption of CO on the bimetallic PdGa@SiO₂ compared to that observed for the monometallic Pd@SiO₂. The CO coverage was chosen in accordance with the experimentally observed values from CO chemisorption.³⁹ 10 CO molecules were placed on the surface of a pre-optimised Pd₁₈Ga₂₀ NP, and the particle was evolved using MTD. A pure Pd NP with 35 CO* was also considered for comparison. CN_{Pd-C} and CN_{Ga-C} were used as additional CVs to model interactions between the PdGa NP with the CO molecules. The structures closest to the free energy minima are shown in Figure 2 a). The FES, the initial guess, and the evolution of the CVs during the MTD simulations can be found in Figures S21-S28.

The minimum free energy structures of the Pd₁₈Ga₂₀(CO)₁₀ NP and Pd₁₈Ga₂₀ NP in vacuum differ significantly. For the Pd₁₈Ga₂₀(CO)₁₀ NP, CO molecules are exclusively bound to the surface and preferentially coordinated to Pd with a CN_{Pd-C} = 0.6 with limited coordination to Ga with CN_{Ga-C} = 0.2 (Figures 2 a) and S28). Meanwhile, the PdGa NP itself undergoes significant structural changes. The formation of a Pd-core within the NP leads to an increased CN_{Pd-Pd} from 2.5 to 3.6 ($\alpha_{\text{Ga-Pd}} = -0.35$ and $\alpha_{\text{Pd-Ga}} = 0.18$). Meanwhile, the migration of Ga to the surface is evidenced by decreased CN_{Pd-Ga} from 3.7 to 2.8 and decreased CN_{Ga-Ga} from 2.3 to 1.4. (compare Figure 1 vs. Figure 2a and S28). The dealloying of Ga to the NP surface is further evidenced by the larger mean distance of Ga to the centre of mass (4.4 Å) compared to Pd (3.2 Å). Importantly, some Pd surface sites are retained and responsible for CO adsorption. The separation of surface Pd atoms by Ga is consistent with CO adsorption IR, which shows no contiguous domains of metallic Pd at the NP surface.^{39,59,60}

The binding mode of the adsorbed CO also changes, as indicated by the CO adsorption IR (Figure 2 b) and 2 c)): For the Pd₃₈(CO)₃₅ NP, a significant amount of surface CO is coordinated in a bridged fashion between multiple Pd atoms. In contrast, the adsorbed CO for Pd₁₈Ga₂₀(CO)₁₀ are predominantly terminal.

To better understand the proportion of different CO binding modes on the surface, AIMD was used to simulate the structure of the particles closest to the minima in the FES at a realistic CO₂ hydrogenation temperature of 503 K. In the simulation, the adsorbates transition rapidly between different coordination environments indicating low activation energies for the transition (Figure S45). Pd₁₈Ga₂₀(CO)₁₀ and Pd₃₈(CO)₃₅ exhibit radically different distributions of the main coordination modes (Figure 2 b) and Table S5). Pd₁₈Ga₂₀(CO)₁₀ shows only terminal CO, while a mixture of terminal and μ_2 -bridging CO is present in Pd₃₈(CO)₃₅. Neither particle shows μ_3 -bridging CO for the selected cut-off distance of 2.3 Å.

To compare these results to experimental CO adsorption IR spectra, the AIMD trajectories were Fourier transformed to obtain simulated IR spectra (Figure 2 c) (i)). The simulated spectrum (Figure 2 c) (i)) of Pd₃₈(CO)₃₅ consists of two dominant absorption bands centred at 2010 and 1870 cm⁻¹, which are attributed to terminal and bridging carbonyls, respectively. This is consistent with the experimental CO-adsorption IR of Pd@SiO₂ (Figure 2 c) (ii)), where two dominant bands are also observed. The maxima of these peaks are found at *ca.* 2090 and 1960 cm⁻¹. The simulated spectrum for Pd₁₈Ga₂₀(CO)₁₀ consists of a single symmetrical band at *ca.* 1970 cm⁻¹, which, based on the observation of exclusively terminal CO in the simulation (Figure 2 b)), and previous assignments, is attributed to terminal Pd-CO species. The experimental spectrum for PdGa@SiO₂ is dominated by a symmetrical peak at 2080 cm⁻¹, with smaller contributions from a broad peak at *ca.* 1950 cm⁻¹, attributed to bridging carbonyl species.

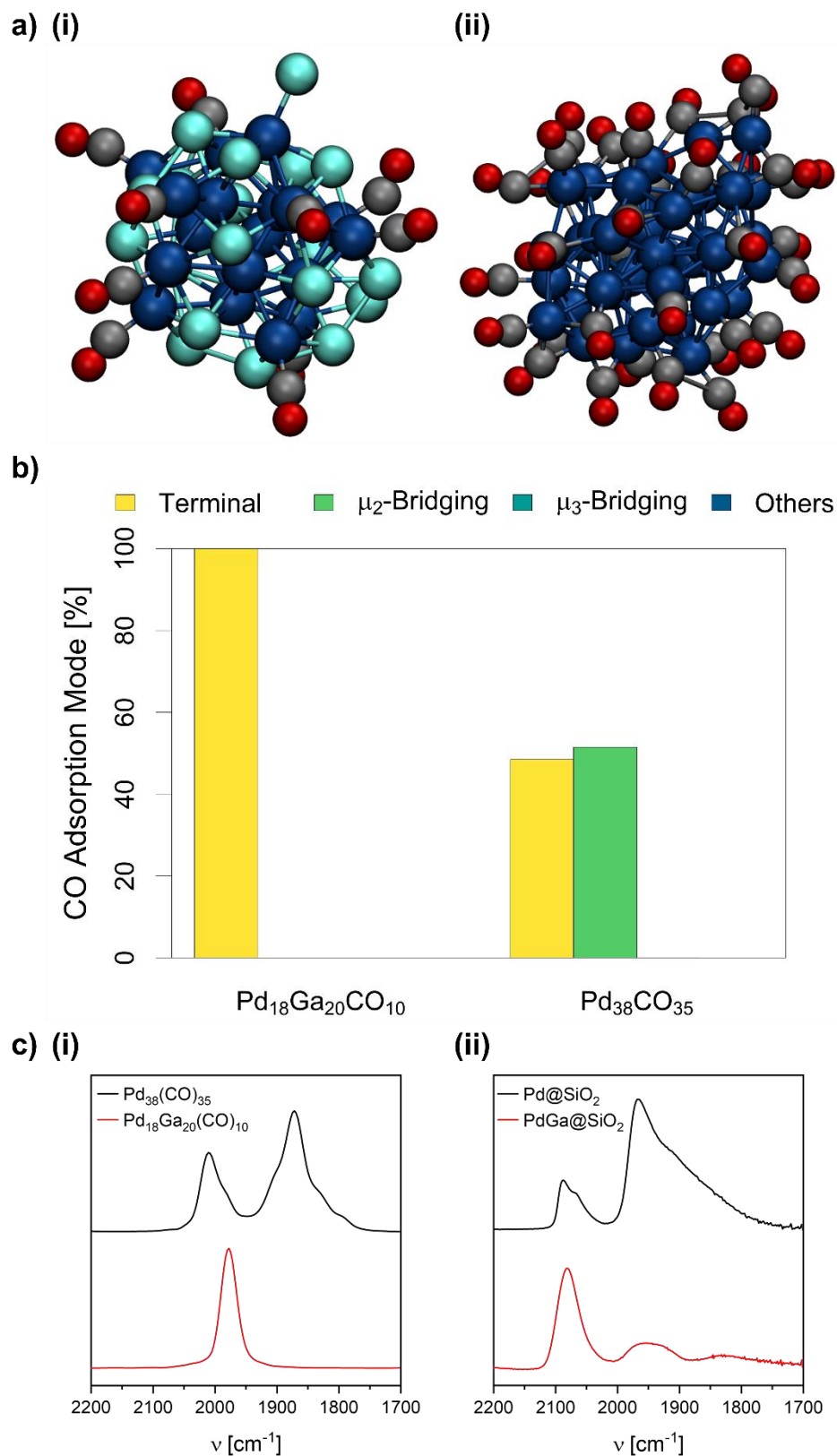


Figure 2: a) Structures of (i) $\text{Pd}_{18}\text{Ga}_{20}(\text{CO})_{10}$ NP and (ii) $\text{Pd}_{38}(\text{CO})_{35}$ NP in vacuum obtained from Metadynamics. Pd: dark blue, Ga: brighter blue, C: black, and O: red (trajectories and FES can be found in Figures S21-S40). b) Proportion of different CO coordination modes of the $\text{Pd}_{18}\text{Ga}_{20}(\text{CO})_{10}$ and $\text{Pd}_{38}(\text{CO})_{35}$ NP obtained from AIMD simulations. c) (i) Simulated IR spectra from the AIMD simulations of the $\text{Pd}_{18}\text{Ga}_{20}(\text{CO})_{10}$ and $\text{Pd}_{38}(\text{CO})_{35}$ NP (ii) Experimental CO-IR for Pd@SiO_2 and PdGa@SiO_2 (Background subtracted).

This disparity between calculation and experiment (i.e. the observation of some bridged species experimentally) may arise from inhomogeneity of the sample, however, the trends in both experiment and simulation are consistent. To summarize, the IR spectra confirm the interaction between CO and PdGa is dominated by terminal CO binding, whereas two frequencies are observed for the Pd NP, corresponding to terminal and bridging CO respectively, which is consistent with the experimental CO adsorption IR.³⁹

Structure of Hydrides on PdGa-Catalysts

Equally important for both reactivity and characterization, but much harder to probe experimentally, are the coordination modes of hydrides during CO₂ hydrogenation and the subsequent structural changes of the NPs. From an experimental perspective, bulk Pd is known to form a sub-surface PdH_x alloy phase, which makes interpretation of H₂ chemisorption challenging in terms of adsorption stoichiometry.^{61,62} Since the simulation of Pd₁₈Ga₂₀ and Pd₃₈ NPs with adsorbed CO successfully reproduced the CO adsorption IR spectra, we reasoned that placing H* onto the NPs could help us understand the binding mode of chemisorbed H*, and the disparities between particle sizes (from TEM) and H₂ uptake (chemisorption). H₂ chemisorption data suggests the coverage is equal to 1.1 H and 1.25 H per Pd for the PdGa and Pd NPs, respectively. Thus, 20 H* and 48 H* atoms were placed on the surface of pre-optimized Pd₁₈Ga₂₀ NP and Pd₃₈ NP, respectively. The evolution of the particles was followed by MTD. CN_{Pd-H} and CN_{Ga-H} were used as additional CVs to model interactions between the PdGa NP and H* atoms.

For the Pd₁₈Ga₂₀H₂₀ NP, all CNs decrease slightly in the most stable structure (CN_{Pd-Pd} from 2.5 to 1.9, CN_{Pd-Ga} from 3.7 to 2.7 and CN_{Ga-Ga} from 2.3 to 1.6, $\alpha_{\text{Ga-Pd}} = -0.36$ and $\alpha_{\text{Pd-Ga}} = 0.07$, Figures 3 and S47-S55). The decrease in CN is attributed to a particle expansion in the presence of hydrides,⁶³⁻⁶⁵ and is further evidenced by the increased distance of metal atoms to the centre of mass of the NP (3.7 Å vs. 3.9 Å, Figure S50). Contrary to the simulations with CO, no dealloying is observed for the PdGa NP with H* (compare Figure 2 vs. Figure 3). In Pd₁₈Ga₂₀H₂₀ NPs, H* atoms are preferentially bound to Pd (CN_{Pd-H} = 1.0) but also to Ga (CN_{Ga-H} = 0.8) (Figures 3 and S55), and the overall coordination number of adsorbed H* is lower than for the pure Pd NP. Conversely, the Pd NP has significant amounts of subsurface hydrides, explaining the high H/Pd stoichiometry. This is well documented for Pd, which is known to adsorb hydrogen to form a bulk PdH_x alloy.^{61,62}

Subsequent AIMD simulations confirm that H* atoms are generally less coordinated in Pd₁₈Ga₂₀H₂₀ compared to the Pd₃₈H₄₈ NP (Figure 3 and Table S7), reminiscent of the simulations with CO. Pd₁₈Ga₂₀H₂₀ shows mainly μ_2 -bridging hydrides with a significant number of terminal hydrides and a small amount of μ_3 -bridging hydrides. In contrast, on the Pd₃₈H₄₈ NP, very few terminal hydrides are observed, with μ_2 -bridging hydrides and μ_3 -bridging hydrides dominating. Moreover, in both cases H* rapidly exchange between different coordination environments indicating low activation energies for the transition between binding sites and binding modes (Figure S73).

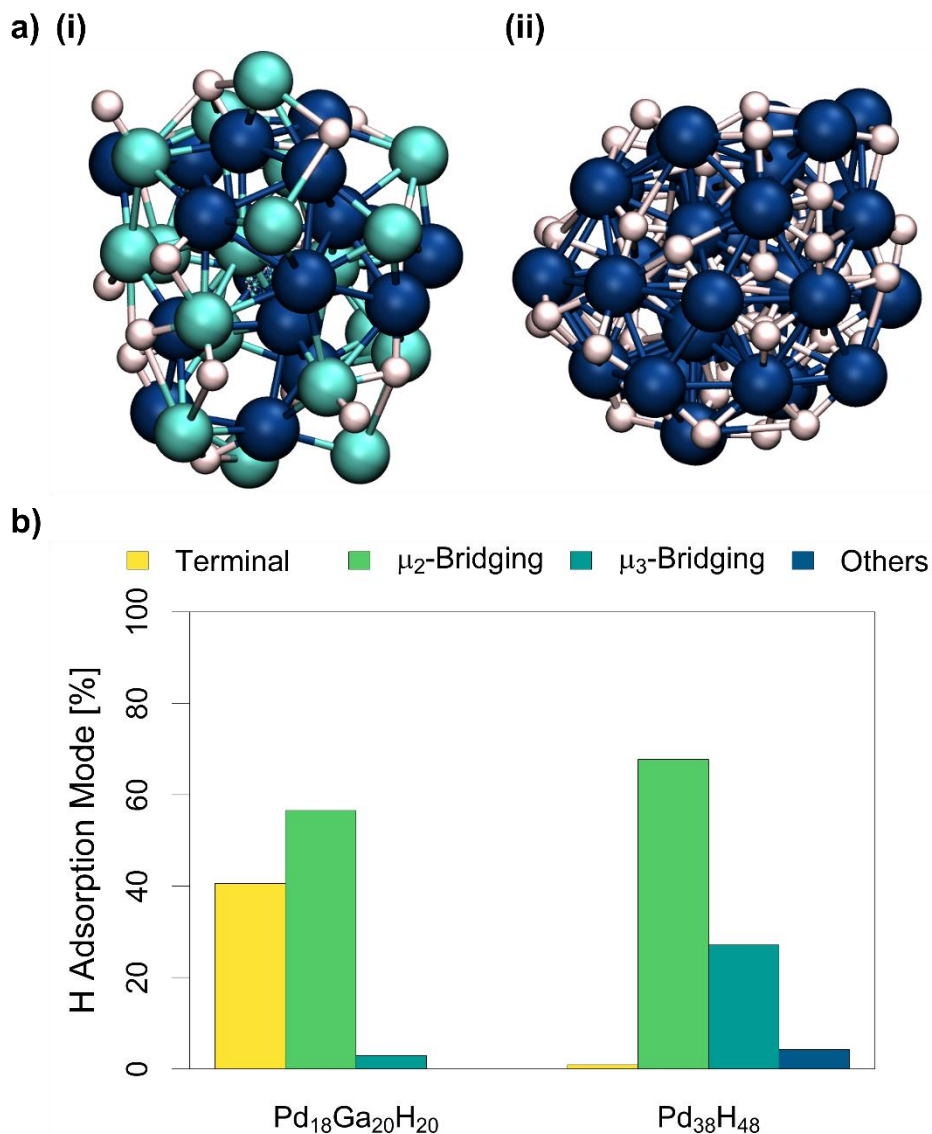


Figure 3. a): Structure of (i) Pd₁₈Ga₂₀H₂₀ NP and (ii) Pd₃₈H₄₈ NP in vacuum obtained from Metadynamics. Pd: dark blue, Ga: brighter blue, and H: white (trajectories and FES can be found in Figures S47-S68). b): Proportion of different hydride coordination modes of the Pd₁₈Ga₂₀H₂₀ and Pd₃₈H₄₈ NP obtained from AIMD simulations.

Influence of Oxygen Chemical Potential and Implications for PdGa NPs under CO_x Hydrogenation Conditions

Next, we assessed how switching to more oxidising (CO₂ hydrogenation) conditions affects the distribution of Ga and Pd within the particle. As recently shown, CO₂ hydrogenation conditions are much more oxidising than the equivalent CO hydrogenation conditions, mainly due to the large quantity of water produced.²⁵ In fact, the Ga K-edge XANES shows that the CO₂ hydrogenation conditions (H₂:Ar:CO₂ (3:1:1)) promote partial oxidation of Ga(0) from the alloyed PdGa NP (Figure 4), as illustrated by the increase in whiteness intensity (10375 eV), and the depletion of the feature at ca. 10368 eV that is indicative of Ga(0).³⁹ Further analysis of the time-resolved process, by means of multivariate curve resolution alternating least squares (MCR-ALS) analysis suggest that this oxidation process occurs rapidly upon introduction of CO₂ (Figure 4). Meanwhile, the average Ga-Pd path degeneracy obtained from fitting of the Ga K-edge EXAFS decreases from 0.7 ± 0.2 to 0.3 ± 0.1 after reaction, while the Ga-O path degeneracy increases from 2.9 ± 0.4 to 3.5 ± 0.3 – indicating that a proportion of the reduced Ga found in the alloyed NPs indeed partially oxidises upon exposure to reaction conditions (Figures S1-S4, Tables S1-S3).

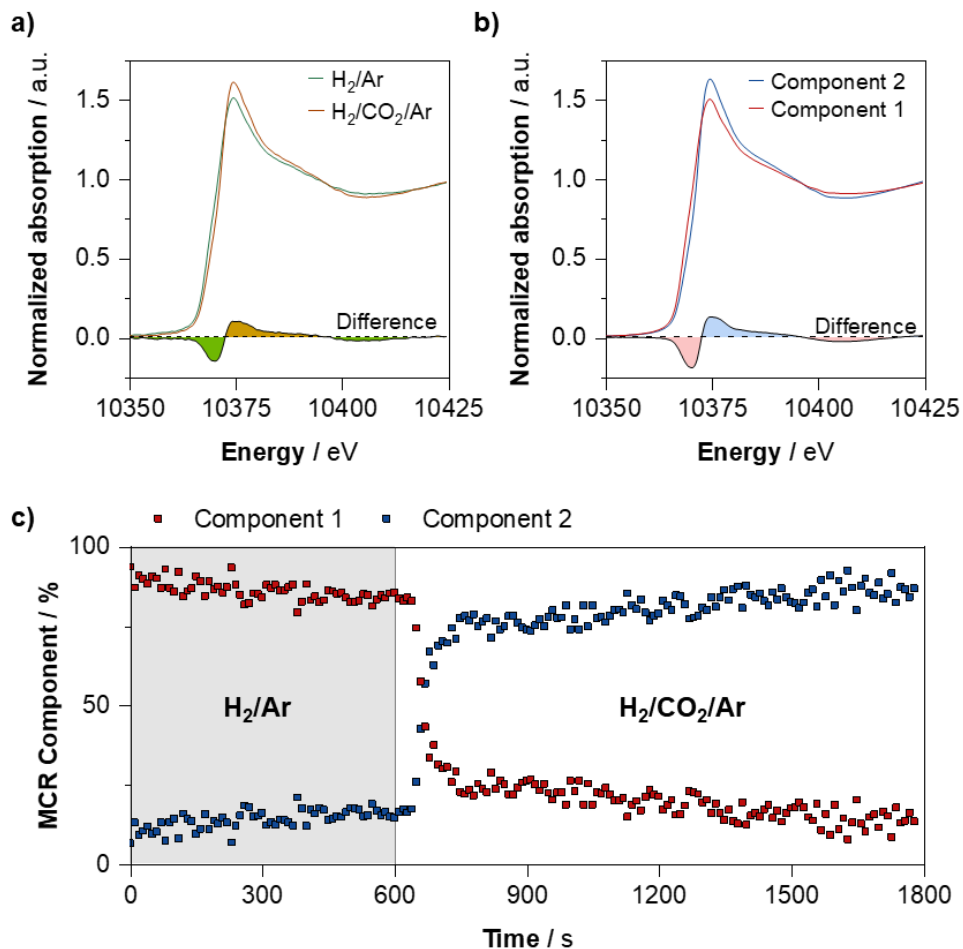


Figure 4: Ga K edge XANES of PdGa@SiO₂ under reaction conditions. a) before and after introduction of CO₂, b) pure spectral components obtained from a 2-component MCR fit tracking introduction of CO₂ into the gas phase, and c) MCR component profiles tracking influence of introduction of CO₂ to the reactive gas mixture.

We thus evaluated the influence of the more “oxidizing” conditions on the structure of the alloy by adding O* atoms that would arise from the reaction of CO₂ or H₂O (Figure S46). Different Pd₁₈Ga₂₀O_x NPs were simulated with various O* contents (X = 10, 20, and 30; 0.5, 1.0, and 1.5 relative to Ga) to gain insights into general structural trends. CN_{Pd-O} and CN_{Ga-O} were used as additional CVs.

Independently of the studied O* contents, CN_{Pd-Ga} and CN_{Ga-Ga} decrease in the presence of O* while CN_{Pd-O} and CN_{Ga-O} increase (Figure 5, Table 1 and Figures S75-S102). While CN_{Pd-Pd} does not vary significantly with different stoichiometries of O*, it increases compared to the pristine PdGa NP. These two observations combined indicate partial dealloying of the NP independently of the oxygen coverage. The large distance of Ga to the centre of mass of the Pd₁₈Ga₂₀O₁₀ NP (4.5 Å) compared to Pd (3.3 Å) once again indicates that Ga is extruded to the surface upon exposure to more oxidizing conditions and that a Pd-rich core is present, causing the increase in CN_{Pd-Pd}.

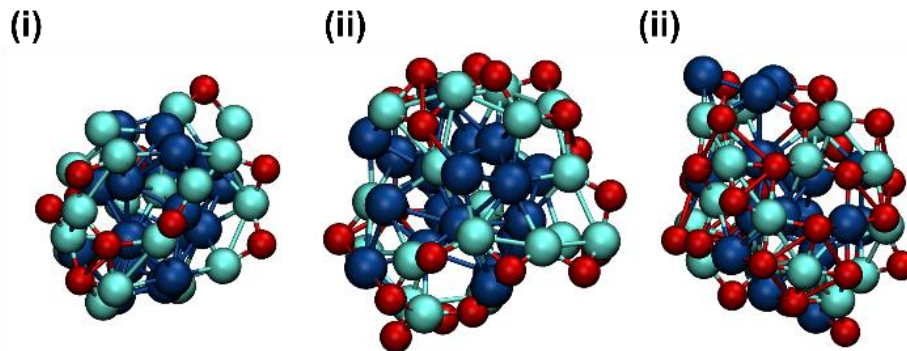


Figure 5: Structure closest to the free energy minima for the (i) $\text{Pd}_{18}\text{Ga}_{20}\text{O}_{10}$ NP, (ii) $\text{Pd}_{18}\text{Ga}_{20}\text{O}_{20}$ NP, and (iii) $\text{Pd}_{18}\text{Ga}_{20}\text{O}_{30}$ NP. The FES, the initial guess for each structure, and the analysis of the trajectories can be found in Figures S75-S102.

Table 1: Values of the $\text{CN}_{\text{Pd-Pd}}$, $\text{CN}_{\text{Pd-Ga}}$, $\text{CN}_{\text{Ga-Ga}}$, $\text{CN}_{\text{Pd-O}}$ and $\text{CN}_{\text{Ga-O}}$ at the minima of the FES of $\text{Pd}_{18}\text{Ga}_{20}$, $\text{Pd}_{18}\text{Ga}_{20}@\text{SiO}_2$, $\text{Pd}_{18}\text{Ga}_{20}\text{O}_{10}$, $\text{Pd}_{18}\text{Ga}_{20}\text{O}_{20}$ and $\text{Pd}_{18}\text{Ga}_{20}\text{O}_{30}$ NPs.

	$\text{Pd}_{18}\text{Ga}_{20}$	$\text{Pd}_{18}\text{Ga}_{20}\text{O}_{10}$	$\text{Pd}_{18}\text{Ga}_{20}\text{O}_{20}$	$\text{Pd}_{18}\text{Ga}_{20}\text{O}_{30}$
$\text{CN}_{\text{Pd-Pd}}$	2.5	3.6	3.4	3.3
$\text{CN}_{\text{Pd-Ga}}$	3.7	2.5	2.5	2.1
$\text{CN}_{\text{Ga-Ga}}$	2.3	1.1	1.3	1.3
$\text{CN}_{\text{Pd-O}}$	-	0.4	0.6	1.1
$\text{CN}_{\text{Ga-O}}$	-	0.7	1.1	1.8

While oxygen is coordinated to both Pd and Ga, a slightly higher $\text{CN}_{\text{Ga-O}}$ of *ca.* 0.5 compared to $\text{CN}_{\text{Pd-O}}$ is observed for all O^* contents, indicating that Ga is preferentially oxidised in these systems, which is consistent with observations from *in-situ* XAS experiments, where oxidation of Ga is observed (Figure 4). However, some Ga remains in close contact with Pd (i.e. $\text{CN}_{\text{Pd-Ga}} > 0$), which suggests that complete oxidation and, therefore, complete dealloying does not occur, even where the oxygen stoichiometry is sufficient to allow full oxidation of Ga into Ga_2O_3 (1.5 O^* per Ga). Instead, the competing interaction of Pd with Ga ($\text{Ga}(0)$ or Ga^{III}) is strong enough to retain some Pd-Ga interaction and prevents the complete oxidation of Ga, which is consistent with experimental observations for $\text{PdGa}@\text{SiO}_2$.

Conclusion

In this work, we showcase how MTD simulations can help to elucidate the structure of small PdGa NPs and how these alloys evolve in active atmospheres, which mimic specific conditions, in particular the relatively oxidising CO_2 hydrogenation conditions. We use AIMD/MTD to show that small Pd and PdGa NPs are dynamic systems, with low barriers for structural rearrangement. In the absence of external reactants, the PdGa NP alloys substantially, likely driven by the strong interaction of Pd with Ga. This results in the dilution of Pd sites on the NP surface. Yet, the alloy does not show any long-range order in the form of crystalline domains. No drastic change in terms of particle structure or shape is observed when the NPs interact with silica, showing that the support can be considered innocent in this system.

In the presence of CO adsorbates, AIMD/MTD simulations confirm experimental findings, e.g. CO binds almost exclusively as terminal CO to isolated Pd sites in the PdGa alloy, while more bridging CO adsorbates are observed on pure Pd. Simulated IR spectra also enabled us to assign the different signals previously observed using CO adsorption IR spectroscopy to the differ-

ent CO binding modes for both Pd and PdGa systems. Regarding the structure of surface hydrides evidenced by H₂ chemisorption, they are calculated to be predominantly bound to Pd in a terminal coordination mode in the presence of Ga, which is associated with a higher reactivity compared to the pure Pd NP.

Finally, under oxidative atmosphere, expected under CO₂ hydrogenation conditions, the PdGa NPs partially dealloy upon the presence of O*, leading to the formation of a Pd-rich core and a partially oxidised GaO_x shell, reconciling previous observations from *in-situ* XAS about the preferential partial oxidation of Ga in PdGa NPs, consistent with the very low standard oxidation potential of Ga compared to that of Pd.⁶⁶ Maximizing Ga-O-interactions therefore drives the dealloying process, resulting in a partially dealloyed PdGa-core with a GaO_x shell. Yet, the complete oxidation of Ga to Ga₂O₃ is not observed, even at high oxygen coverage, which indicates strong interaction of the partially oxidised GaO_x with the Pd. Such behaviour is reminiscent of strong metal-support interaction, which can cause charge transfer from the support to the metal and result in significant changes in the activity of the metal.⁶⁷⁻⁷⁰ Strong metal-support interaction typically results in encapsulation of the metal NPs with the oxide supports. However, our simulations suggest in the case of very small NPs and a small amount of adsorbed oxygen in the system, some of the metal alloy surface remains accessible for further reactions with the gas phase.

Overall, these results demonstrate that the structure of alloyed PdGa NPs is highly dynamic and sensitive to the surrounding atmosphere, likely enabling rapid changes and (de)alloying under reducing and oxidizing conditions. This work also highlights how MTD is a powerful approach to elucidate structural dynamics at a single particle level, such as the dynamics of adsorbed hydrides, while static computations with slab models or small clusters would not be able to capture these changes. We are investigating further implications of these results and how they can be generalised to other catalytic systems and reaction conditions and will report our results in due course.

Computational and Experimental Methods

Models for Pd and PdGa NPs (0.8 nm, 38 atoms) were constructed, which have a size comparable to the synthesised NPs (1.6 ± 0.4 nm).³⁹ The crystalline PdGa NP was constructed by cutting the bcc-PdGa bulk structure at different low-index facets and used as a starting guess (Figure 1 b) (i), Pd is shown in dark blue while Ga is shown in brighter blue). Surface interactions were captured by using a model surface of dehydroxylated amorphous SiO₂₋₇₀₀ (silica model with an OH-density similar to silica dehydroxylated at 700 °C, which used to synthesise the PdGa NPs)³⁹ previously developed.⁵⁸

Calculations were carried out with the CP2K package.⁷¹⁻⁷⁸ Periodic Kohn-Sham Density-Functional Theory (DFT) was used with the exchange-correlation functional of Perdew, Burke, and Ernzerhof (PBE) in the rev-PBE implementation.⁷⁹⁻⁸³ Additional Grimme dispersion corrections with Beckett-Johnson damping function (D3-BJ) were employed.^{84,85} A Gaussian plane wave (GPW) basis set on the DZVP level was employed.^{86,87} Goedecker-Teter-Hutter (GTH) pseudopotentials were chosen to model core electrons.⁸⁸⁻⁹² The SiO₂₋₇₀₀ support was modelled using an SZV GPW basis set.^{86,87}

AIMD was used in the Born-Oppenheimer variant to explore the conformational space of the NPs.^{42,93} All calculations were carried out in an NVT (canonical) ensemble held at the reaction temperature of 503 K. The temperature was imposed using the canonical sampling through velocity rescaling thermostat with a time constant of 100 fs.⁹⁴ Hydrogen was replaced by deuterium to avoid artificial bond breaking due to the fast motion of H. The AIMD time steps were chosen as 1 fs. For simulations of the SiO₂ surface, atoms from the lower half of the support were frozen.

MTD was employed with the Lagrangian formulation to accelerate the AIMD runs and explore the conformational space of the PdGa NP more efficiently.⁴³⁻⁴⁷ Gaussian-shaped potentials (hills) were deposited along the CVs every 20 steps (every 20 fs) with a height of 0.01 Hartree (Ha). The width was chosen as 0.15 times the range of the CVs. This compromise minimizes the overall error on the FES made between deposited Gaussian size and simulation time.^{47,95} Simulations for the conformational analysis of the NPs (unsupported and supported, with and without adsorbates) were run for 20 ps.

The correct choice of CVs is very important for MTD. It is required for them to distinguish between all intermediates to map them on the FES unambiguously. The coordination number between two elements X and Y (CN_{X-Y}) is commonly chosen as a CV, as shown in equation (1).⁹⁶

$$CN_{X-Y} = \frac{1}{n_X} \cdot \sum_{i_X, j_Y}^{n_X, n_Y} \left[\frac{1 - \left(\frac{r_{i_X, j_Y}}{r_{X-Y}^0} \right)^{nn_{X-Y}}}{1 - \left(\frac{r_{i_X, j_Y}}{r_{X-Y}^0} \right)^{nd_{X-Y}}} \right] \quad (1)$$

Here, r_{X-Y}^0 is the cut-off distance, r_{i_X, j_Y} is the distance between the atoms i_X and j_Y and the exponents nn_{X-Y} and nd_{X-Y} determine the steepness of the cut-off. To find the optimum values, the trajectory of the PdGa NP was analysed with r^0 values ranging from $r_{X-Y}^0 = 1.0 \text{ \AA}$ to 5.0 \AA , nn values ranging from $nn_{X-Y} = 5$ to 20 and nd values ranging from $nn_{X-Y} = 10$ to 25 (Figure S5). It was found that the qualitative results are not strongly dependent on the exact choices of the parameters of the CVs, as long as the values are in a reasonable range around the optimal values, as claimed by Valsson *et al.*⁹⁷ For the simulations, $nn_{X-Y} = 6$ and $nd_{X-Y} = 12$ were chosen for all CN values since they provide a good trade-off between sharp transitions at the cut-off distance and smooth CN values. The coordination number of Pd to Pd (CN_{Pd-Pd} , $r_{Pd-Pd}^0 = 3.0 \text{ \AA}$) and Ga (CN_{Pd-Ga} , $r_{Pd-Ga}^0 = 2.8 \text{ \AA}$) as well as Ga to Ga (CN_{Ga-Ga} , $r_{Ga-Ga}^0 = 2.8 \text{ \AA}$) were used to explore the conformational space of the PdGa NPs. For subsequent Metadynamics simulations, the coordination to C (from CO) (CN_{M-C} , $r_{M-C}^0 = 2.1 \text{ \AA}$), to D (as a replacement to H) (CN_{M-D} , $r_{M-D}^0 = 1.9 \text{ \AA}$) and to O (CN_{M-O} , $r_{M-O}^0 = 2.0 \text{ \AA}$) with $M = \text{Ga, Pd}$ were considered as well. The cut-off distances r_{X-Y}^0 were chosen to be around 1.3 times the sum of the Van-der-Waals radii of the individual atoms and allow good differentiation between bound atom pairs ($r_{i_X, j_Y} < r_{X-Y}^0$), unbound atom pairs ($r_{i_X, j_Y} > r_{X-Y}^0$) and intermediate states ($r_{i_X, j_Y} \approx r_{X-Y}^0$). All CVs were added to the extended Lagrangian with $\lambda = 0.5$ and restricted to positive values by a quartic wall at 0 to prevent negative, non-physical CNs.

For a better understanding of the specific properties of the trajectories, such as the movement of particular atoms in the particle or the connectivity of surface adsorbates to compare AIMD and MTD, the trajectories were post-treated with the PLUMED library.^{98,99} For the analysis of the AIMD trajectories in the presence of adsorbates, CNs of adsorbates ($X = \text{C, H}$) to the metal atom (CN_{X-M} , $M = \text{Pd, Ga}$) were recorded and categorized into terminal ($0.5 < CN_{X-M} < 1.5$), μ_2 -bridging ($1.5 < CN_{X-M} < 2.5$), μ_3 -bridging ($2.5 < CN_{X-M} < 3.5$) and subsurface (internal) ($3.5 < CN_{X-M}$). Cut-off distances of $r_{H-M}^0 = 2.1 \text{ \AA}$ and of $r_{C-M}^0 = 2.3 \text{ \AA}$ were chosen to categorize the CN_{X-M} . Analysis of various cut-off distances indicated that while the relative amounts of the different categories depend on the cut-off distance, the overall trends between Pd and PdGa NP are independent of the cut-off distance as long as the cut-off distances are not too short ($r_{C-M}^0 > 2.1 \text{ \AA}$ and $r_{H-M}^0 > 1.7 \text{ \AA}$, compare Figures S42, S45, S70 and S73).

The IR-spectra were calculated using TRAVIS (TRajjectory Analyzer and VISualizer), a free program package for analysing and visualising Monte Carlo and molecular dynamics trajectories.^{100,101} The dipole moments were calculated using the Voronoi tessellation, as implemented in CP2K, and exported as BQB files, which are produced using an efficient lossless compression algorithm for trajectories of atom positions and volumetric data.¹⁰²⁻¹⁰⁷

In addition to the previously mentioned coordination number, we also investigated different CVs to better distinguish different states. We first evaluated the influences of the three primary parameters on the CNs (nn , nd , and r^0). The chosen parameters are sufficiently close to the ideal values since small changes in the parameters have a somewhat limited influence on the CVs. We refer the reader to the SI for the complete analysis (Figure S5). We also looked at other CVs for the trajectories. This includes the CNs of each atom (to specific elements and to all other atoms), the interatomic distances, the distance to the C-O-M (Centre of Mass), and the cluster size of each metal in the NPs with and without oxygen/hydrogen using contact matrices,

where the CNs are used as switching functions. The hills of the MTD run were also summed up using PLUMED to generate the FES. For better comparison of the MTD runs, the FES were normalised; the total free energy of one NP is divided by the number of metal atoms in the NP to obtain the free energy per mole of Metal in the NP, denoted as kcal/mol_M.

The MTD runs were visualised using Visual Molecular Dynamics (VMD), a molecular visualization program for displaying, animating, and analysing larger large biomolecular systems or particles.¹⁰⁸ It is available free of charge (including source code) on their Website. The images were exported using the Tachyon ray tracing library built into VMD.¹⁰⁹

The materials described (PdGa@SiO₂ and Pd@SiO₂) were prepared according to a reported procedure.³⁹ Fitting of the Ga K edge EXAFS was performed on previously published data.³⁹ For Ga K edge EXAFS, the amplitude reduction factor (S_0^2) was not specifically extracted, meaning that coordination numbers will be systematically underestimated, but trends across EXAFS fitting will be consistent within the series of measurements. The program package Demeter was used for fitting of EXAFS.¹¹⁰ Time-resolved XAS at the Ga K edge was measured at the SuperXAS beamline (X10DA) at the Swiss Light Source (SLS, PSI, Villigen, Switzerland), operating in top-up mode at a 2.4-GeV electron energy and a current of 400 mA. Calibration of the monochromator energy at the Ga K edge was achieved using a Zn foil (9659 eV) as an in-line reference, placed between the second and third ion chambers. The incident photon beam was selected by a liquid nitrogen-cooled Si (111) quick-EXAFS monochromator, and the rejection of higher harmonics and focusing were achieved by a rhodium-coated collimating mirror. The beam size on the sample was approximately 2000 μm x 500 μm . During measurement, the quick XAS monochromator was rotating (1 Hz, 2.5° angular range) and spectra were collected in transmission mode using ionization chambers specially developed for quick data collection.

For *in-situ* XAS experiments, the air-exposed powder sample (ca. 20 mg, 250-400 μm SiO₂ aggregates) was packed into quartz capillary (3 mm $\varnothing_{\text{outer}}$, 2.8 mm $\varnothing_{\text{inner}}$, bed length ca. 1 cm) which was integrated to a pressurisable gas flow system consisting of 2 parallel arrays, each consisting of 3 mass flow controllers (MFCs, Bronkhorst), while the total pressure was maintained by a back-pressure regulator (Bronkhorst EL-Press). Switching between the two systems (i.e. switching the MFC array that was feeding the capillary) was performed using a remote controlled 6-port 2-way switching valve (VICI, Valco) that could be operated from outside the experimental hutch. While one gas mixture was flowing to the cell, the other was directed via a bypass to the exhaust. Samples were heated using a custom-built infrared heater (Elstein-Werk M. Steinmetz GmbH & Co. KG (Germany), 30 mm length, with two heating elements – one above and one below sample capillary), and temperature was monitored/maintained using a 0.3-mm K-type thermocouple placed in direct contact with the catalyst bed. Ar and H₂ were purified by passing through a trap containing molecular sieves and Q5 catalyst prior to introduction to the XAS quartz cell. CO₂ was purified by passing through a trap containing molecular sieves.

In the *in-situ* experiment, Ar (10 sccm, 1 bar) was flowed over the over the catalyst for 10 minutes while the spectra were recorded. The gas flow was then changed to H₂ (10 sccm, 1 bar), and the sample was heat-treated to 300 °C with a ramp of 5 °C min⁻¹, before cooling to 230 °C. Spectra were recorded continuously during the hydrogen treatment. The gas composition was then switched to H₂/Ar (3:2, 10 sccm), and subsequently pressurized to 11 bar. At the point at which pressure stabilized, acquisition was started, and the sample was measured continuously for 30 minutes. After 10 minutes of acquisition, the gas composition was switched, under isobaric conditions, using the 6-port valve, to H₂/Ar/CO₂ (3:1:1, 10 sccm), to capture any changes upon introduction of CO₂ to the reaction gas. The delay between switching of the gas compositions and CO₂ reaching the catalyst bed was estimated to be approximately 40 seconds, based on the reduced absorption of the beam (drop in baseline of spectrum prior to normalization) upon replacing a fraction of the Ar in the feed with less-absorbing CO₂, using a strategy similar to that described by Lomachenko, *et al.*¹¹¹ Multivariate curve resolution alternating least-squares (MCR-ALS) analysis is a chemometric method that enables the extraction of the concentration profiles of pure components of complex

mixtures on the basis of their kinetic behaviour (i.e. a response to an applied stimulus).^{112,113} Thus, it is well-suited to tracking the distribution of kinetically-distinct species during *in-situ* experiments.^{114,115} MCR-ALS algorithm is used to decompose a series of experimental spectra (D) into pure contributions, consisting of concentration profiles (C) and the corresponding spectra (S) of different chemical compounds, based on the equation $D = CS^T + E$, where S^T is the transpose of matrix S and E corresponds to the residual. For this purpose, the in-built MCR feature of the ProQEXAFS software was used.¹¹⁶ For the analysis, an energy range of 10300-10450 eV was used for the Ga K-edge. Spectra were first normalized and cut to include only the relevant range for further analysis.

ASSOCIATED CONTENT

Supporting Information. Additional Figures and the Trajectories of the MTD/AIMD runs. Additional XAS and further details of XAS experiments.

AUTHOR INFORMATION

Corresponding Author

* Christophe Copéret, ccoperet@inorg.chem.ethz.ch

* Pierre-Adrien Payard, pierre-adrien.payard@univ-lyon1.fr

Author Contributions

¶ J.F.B., A.M. and S.R.D. contributed equally to this work. J.F.B. and A.M. performed the calculations. S.R.D. performed XAS analysis. The manuscript was written through the contributions of all authors. All authors have given approval to the final version of the manuscript.

Funding Sources

This research is supported by the Sinergia Project of the Swiss National Science Fonds (SNSF fond number: CRSII5_183495). C.C. and S.R.D. acknowledge the Swiss National Science Foundation (grants 200021_169134, and 200020B_1920) Aleix Comas-Vives thanks the Spanish "Ministerio de Ciencia, Innovación y Universidades" (PID2021-128416NB-I00).

ACKNOWLEDGMENT

We thank Quentin Pessemesse for helping with the data visualisation, imaging of the NPs and calculating the IR-spectra. We acknowledge the Swiss Light Source for beamtime (SuperXAS beamline (X10DA) (Proposal No. 20210709)), and thank Dr. Olga Safonova and Ilia Sadykov for support during the beamtime, as well as members of the Copéret group for their support during these experiments.

REFERENCES

- (1) Fechet, I.; Wang, Y.; Védrine, J. C. The past, present and future of heterogeneous catalysis. *Catal. Today* **2012**, *189* (1), 2–27.
- (2) Liu, L.; Corma, A. Metal Catalysts for Heterogeneous Catalysis: From Single Atoms to Nanoclusters and Nanoparticles. *Chem. Rev.* **2018**, *118* (10), 4981–5079.
- (3) Adams, C. Applied Catalysis: A Predictive Socioeconomic History. *Top. Catal.* **2009**, *52* (8), 924–934.
- (4) Bonrath, W.; Netscher, T. Catalytic processes in vitamins synthesis and production. *Appl. Catal. A: Gen.* **2005**, *280* (1), 55–73.
- (5) Liao, H.; Fisher, A.; Xu, Z. J. Surface Segregation in Bimetallic Nanoparticles: A Critical Issue in Electrocatalyst Engineering. *Small* **2015**, *11* (27), 3221–3246.
- (6) Dang-Bao, T.; Pla, D.; Favier, I.; Gómez, M. Bimetallic Nanoparticles in Alternative Solvents for Catalytic Purposes. *Catalysts* **2017**, *7* (7).
- (7) Loza, K.; Heggen, M.; Epple, M. Synthesis, Structure, Properties, and Applications of Bimetallic Nanoparticles of Noble Metals. *Adv. Funct. Mater.* **2020**, *30* (21), 1909260.
- (8) Wei, R.; Tang, N.; Jiang, L.; Yang, J.; Guo, J.; Yuan, X.; Liang, J.; Zhu, Y.; Wu, Z.; Li, H. Bimetallic nanoparticles meet polymeric carbon nitride: Fabrications, catalytic applications and perspectives. *Coord. Chem. Rev.* **2022**, *462*, 214500.
- (9) Dlamini, N. G.; Basson, A. K.; Pullabhotla, V. S. R. Synthesis and Characterization of Various Bimetallic Nanoparticles and Their Application. *Applied Nano* **2023**, *4* (1), 1–24.
- (10) Liu, X.; Gu, Q.; Zhang, Y.; Xu, X.; Wang, H.; Sun, Z.; Cao, L.; Sun, Q.; Xu, L.; Wang, L.; Li, S.; Wei, S.; Yang, B.; Lu, J. Atomically Thick Oxide Overcoating Stimulates Low-Temperature Reactive Metal-Support Interactions for Enhanced Catalysis. *J. Am. Chem. Soc.* **2023**, *145* (12), 6702–6709.
- (11) Frey, H.; Beck, A.; Huang, X.; van Bokhoven, J. A.; Willinger, M. G. Dynamic interplay between metal nanoparticles and oxide support under redox conditions. *Science* **2022**, *376* (6596), 982–987.
- (12) Beck, A.; Zabilskiy, M.; Newton, M. A.; Safonova, O.; Willinger, M. G.; van Bokhoven, J. A. Following the structure of copper-zinc-alumina across the pressure gap in carbon dioxide hydrogenation. *Nat. Catal.* **2021**, *4* (6), 488–497.
- (13) Urakawa, A. Mind the gaps in CO₂-to-methanol. *Nat. Catal.* **2021**, *4* (6), 447–448.
- (14) Müller, A.; Comas-Vives, A.; Copéret, C. Ga and Zn increase the oxygen affinity of Cu-based catalysts for the CO_x hydrogenation according to ab initio atomistic thermodynamics. *Chem. Sci.* **2022**, *13* (45), 13442–13458.
- (15) Schlögl, R. Heterogeneous Catalysis. *Angew. Chem. Int. Ed.* **2015**, *54* (11), 3465–3520.
- (16) Olah, G. A. Beyond Oil and Gas: The Methanol Economy. *Angew. Chem. Int. Ed.* **2005**, *44* (18), 2636–2639.
- (17) Goeppert, A.; Czaun, M.; Jones, J.-P.; Surya Prakash, G. K.; Olah, G. A. Recycling of carbon dioxide to methanol and derived products – closing the loop. *Chem. Soc. Rev.* **2014**, *43* (23), 7995–8048.
- (18) Magda, R.; Toth, J. The Connection of the Methanol Economy to the Concept of the Circular Economy and Its Impact on Sustainability. *Visegr. J. Bioecon. Sustain. Dev.* **2019**, *8* (2), 58–62.
- (19) Kar, S.; Goeppert, A.; Prakash, G. K. S. Integrated CO₂ Capture and Conversion to Formate and Methanol: Connecting Two Threads. *Acc. Chem. Res.* **2019**, *52* (10), 2892–2903.
- (20) Simon Araya, S.; Liso, V.; Cui, X.; Li, N.; Zhu, J.; Sahlin, S. L.; Jensen, S. H.; Nielsen, M. P.; Kær, S. K. A Review of The Methanol Economy: The Fuel Cell Route. *Energies* **2020**, *13* (3).
- (21) Nakamura, J.; Choi, Y.; Fujitani, T. On the Issue of the Active Site and the Role of ZnO in Cu/ZnO Methanol Synthesis Catalysts. *Top. Catal.* **2003**, *22* (3), 277–285.
- (22) Kuld, S.; Thorhauge, M.; Falsig, H.; Elkjær, C. F.; Helveg, S.; Chorkendorff, I.; Sehested, J. Quantifying the promotion of Cu catalysts by ZnO for methanol synthesis. *Science* **2016**, *352* (6288), 969–974.
- (23) Behrens, M.; Studt, F.; Kasatkin, I.; Kühl, S.; Hävecker, M.; Abild-Pedersen, F.; Zander, S.; Girgsdies, F.; Kurr, P.; Knief, B.-L.; Tovar, M.; Fischer, R. W.; Nørskov, J. K.; Schlögl, R. The Active Site of Methanol Synthesis over Cu/ZnO/Al₂O₃ Industrial Catalysts. *Science* **2012**, *336* (6083), 893–897.
- (24) Lunkenbein, T.; Schumann, J.; Behrens, M.; Schlögl, R.; Willinger, M. G. Formation of a ZnO Overlayer in Industrial Cu/ZnO/Al₂O₃ Catalysts Induced by Strong Metal-Support Interactions. *Angew. Chem. Int. Ed.* **2015**, *54* (15), 4544–4548.

- (25) Kattel, S.; Ramírez, P. J.; Chen, J. G.; Rodriguez, J. A.; Liu, P. Active sites for CO₂ hydrogenation to methanol on Cu/ZnO catalysts. *Science* **2017**, *355* (6331), 1296–1299.
- (26) Pelletier, J. D. A.; Basset, J.-M. Catalysis by Design: Well-Defined Single-Site Heterogeneous Catalysts. *Acc. Chem. Res.* **2016**, *49* (4), 664–677.
- (27) Copéret, C.; Comas-Vives, A.; Conley, M. P.; Estes, D. P.; Fedorov, A.; Mougel, V.; Nagae, H.; Núñez-Zarur, F.; Zhizhko, P. A. Surface Organometallic and Coordination Chemistry toward Single-Site Heterogeneous Catalysts: Strategies, Methods, Structures, and Activities. *Chem. Rev.* **2016**, *116* (2), 323–421.
- (28) Copéret, C.; Fedorov, A.; Zhizhko, P. A. Surface Organometallic Chemistry: Paving the Way Beyond Well-Defined Supported Organometallics and Single-Site Catalysis. *Catal. Letters* **2017**, *147* (9), 2247–2259.
- (29) Samantaray, M. K.; Pump, E.; Bendjeriou-Sedjerari, A.; D'Elia, V.; Pelletier, J. D. A.; Guidotti, M.; Psaro, R.; Basset, J.-M. Surface organometallic chemistry in heterogeneous catalysis. *Chem. Soc. Rev.* **2018**, *47* (22), 8403–8437.
- (30) Copéret, C. Single-Sites and Nanoparticles at Tailored Interfaces Prepared via Surface Organometallic Chemistry from Thermolytic Molecular Precursors. *Acc. Chem. Res.* **2019**, *52* (6), 1697–1708.
- (31) Docherty, S. R.; Copéret, C. Deciphering Metal–Oxide and Metal–Metal Interplay via Surface Organometallic Chemistry: A Case Study with CO₂ Hydrogenation to Methanol. *J. Am. Chem. Soc.* **2021**, *143* (18), 6767–6780.
- (32) Docherty, S. R.; Rochlitz, L.; Payard, P.-A.; Copéret, C. Heterogeneous alkane dehydrogenation catalysts investigated via a surface organometallic chemistry approach. *Chem. Soc. Rev.* **2021**, *50* (9), 5806–5822.
- (33) Noh, G.; Lam, E.; Bregante, D. T.; Meyet, J.; Šot, P.; Flaherty, D. W.; Copéret, C. Lewis Acid Strength of Interfacial Metal Sites Drives CH₃OH Selectivity and Formation Rates on Cu-Based CO₂ Hydrogenation Catalysts. *Angew. Chem. Int. Ed.* **2021**, *60* (17), 9650–9659.
- (34) Lam, E.; Noh, G.; Chan, K. W.; Larmier, K.; Lebedev, D.; Searles, K.; Wolf, P.; Safonova, O. V.; Copéret, C. Enhanced CH₃OH Selectivity in CO₂ Hydrogenation Using Cu-based Catalysts Generated via SOMC from Ga^{III} Single-Sites. *Chem. Sci.* **2020**, *11* (29), 7593–7598.
- (35) Lam, E.; Noh, G.; Larmier, K.; Safonova, O. V.; Copéret, C. CO₂ hydrogenation on Cu-catalysts generated from Zn^{II} single-sites: Enhanced CH₃OH selectivity compared to Cu/ZnO/Al₂O₃. *J. Catal.* **2021**, *394*, 266–272.
- (36) Zhu, H.; Anjum, D. H.; Wang, Q.; Abou-Hamad, E.; Emsley, L.; Dong, H.; Laveille, P.; Li, L.; Samal, A. K.; Basset, J.-M. Sn surface-enriched Pt–Sn bimetallic nanoparticles as a selective and stable catalyst for propane dehydrogenation. *J. Catal.* **2014**, *320*, 52–62.
- (37) Rochlitz, L.; Searles, K.; Alfke, J.; Zemlyanov, D.; Safonova, O. V.; Copéret, C. Silica-supported, narrowly distributed, subnanometric Pt–Zn particles from single sites with high propane dehydrogenation performance. *Chem. Sci.* **2020**, *11* (6), 1549–1555.
- (38) Margossian, T.; Larmier, K.; Kim, S. M.; Krumeich, F.; Fedorov, A.; Chen, P.; Müller, C. R.; Copéret, C. Molecularly Tailored Nickel Precursor and Support Yield a Stable Methane Dry Reforming Catalyst with Superior Metal Utilization. *J. Am. Chem. Soc.* **2017**, *139* (20), 6919–6927.
- (39) Docherty, S. R.; Phongprueksathat, N.; Lam, E.; Noh, G.; Safonova, O. V.; Urakawa, A.; Copéret, C. Silica-Supported PdGa Nanoparticles: Metal Synergy for Highly Active and Selective CO₂-to-CH₃OH Hydrogenation. *JACS Au* **2021**, *1* (4), 450–458.
- (40) Amann, P.; Klötzer, B.; Degerman, D.; Köpfle, N.; Götsch, T.; Lömker, P.; Rameshan, C.; Ploner, K.; Bikaljevic, D.; Wang, H.-Y.; Soldemo, M.; Shipilin, M.; Goodwin, C. M.; Gladh, J.; Halldin Stenlid, J.; Börner, M.; Schlueter, C.; Nilsson, A. The state of zinc in methanol synthesis over a Zn/ZnO/Cu(211) model catalyst. *Science* **2022**, *376* (6593), 603–608.
- (41) Dalebout, R.; Barberis, L.; Totarella, G.; Turner, S. J.; La Fontaine, C.; Groot, F. M. F. de; Carrier, X.; van der Eerden, A. M. J.; Meirer, F.; Jongh, P. E. de. Insight into the Nature of the ZnO x Promoter during Methanol Synthesis. *ACS Catal.* **2022**, *12* (11), 6628–6639.
- (42) Car, R.; Parrinello, M. Unified Approach for Molecular Dynamics and Density-Functional Theory. *Phys. Rev. Lett.* **1985**, *55* (22), 2471–2474.
- (43) Laio, A.; Parrinello, M. Escaping free-energy minima. *Proc. Natl. Acad. Sci.* **2002**, *99* (20), 12562–12566.
- (44) Iannuzzi, M.; Laio, A.; Parrinello, M. Efficient Exploration of Reactive Potential Energy Surfaces Using Car-Parrinello Molecular Dynamics. *Phys. Rev. Lett.* **2003**, *90* (23), 238302.
- (45) Laio, A.; Gervasio, F. L. Metadynamics: a Method to Simulate Rare Events and Reconstruct the Free Energy in Biophysics, Chemistry and Material Science. *Rep. Prog. Phys.* **2008**, *71* (12), 126601.
- (46) Bussi, G.; Laio, A. Using Metadynamics to Explore Complex Free-Energy Landscapes. *Nat. Rev. Phys.* **2020**, *2* (4), 200–212.
- (47) Barducci, A.; Bonomi, M.; Parrinello, M. Metadynamics. *Wiley Interdiscip. Rev. Comput. Mol. Sci.* **2011**, *1* (5), 826–843.

- (48) Payard, P.-A.; Rochlitz, L.; Searles, K.; Foppa, L.; Leuthold, B.; Safonova, O. V.; Comas-Vives, A.; Copéret, C. Dynamics and Site Isolation: Keys to High Propane Dehydrogenation Performance of Silica-Supported PtGa Nanoparticles. *JACS Au* **2021**, *1* (9), 1445–1458.
- (49) Rochlitz, L.; Pessemeesse, Q.; Fischer, J. W. A.; Klose, D.; Clark, A. H.; Plodinec, M.; Jeschke, G.; Payard, P.-A.; Copéret, C. A Robust and Efficient Propane Dehydrogenation Catalyst from Unexpectedly Segregated Pt₂Mn Nanoparticles. *J. Am. Chem. Soc.* **2022**, *144* (29), 13384–13393.
- (50) Couchman, P. R.; Jesser, W. A. Thermodynamic theory of size dependence of melting temperature in metals. *Nature* **1977**, *269* (5628), 481–483.
- (51) Puri, P.; Yang, V. Effect of Particle Size on Melting of Aluminum at Nano Scales. *J. Phys. Chem. C* **2007**, *111* (32), 11776–11783.
- (52) Jiang, H.; Moon, K.; Dong, H.; Hua, F.; Wong, C. P. Size-dependent melting properties of tin nanoparticles. *Chem. Phys. Lett.* **2006**, *429* (4), 492–496.
- (53) Cowley, J. M. An Approximate Theory of Order in Alloys. *Phys. Rev.* **1950**, *77* (5), 669–675.
- (54) Cowley, J. M. Short- and Long-Range Order Parameters in Disordered Solid Solutions. *Phys. Rev.* **1960**, *120* (5), 1648–1657.
- (55) Cowley, J. M. Short-Range Order and Long-Range Order Parameters. *Phys. Rev.* **1965**, *138* (5A), A1384–A1389.
- (56) Frenkel, A. I.; Wang, Q.; Sanchez, S. I.; Small, M. W.; Nuzzo, R. G. Short range order in bimetallic nanoalloys: An extended X-ray absorption fine structure study. *J. Chem. Phys.* **2013**, *138* (6), 64202.
- (57) Kaul, I.; Ghosh, P. First principles investigations of small bimetallic PdGa clusters as catalysts for hydrogen dissociation. *Chem. Phys.* **2017**, *487*, 87–96.
- (58) Comas-Vives, A. Amorphous SiO₂ Surface Models: Energetics of the Dehydroxylation Process, Strain, ab initio Atomistic Thermodynamics and IR Spectroscopic Signatures. *Phys. Chem. Chem. Phys.* **2016**, *18* (10), 7475–7482.
- (59) Kovnir, K.; Armbrüster, M.; Teschner, D.; Venkov, T. V.; Szentmiklósi, L.; Jentoft, F. C.; Knop-Gericke, A.; Grin, Y.; Schlögl, R. In situ surface characterization of the intermetallic compound PdGa – A highly selective hydrogenation catalyst. *Surf. Sci.* **2009**, *603* (10), 1784–1792.
- (60) Sun, Q.; Chen, B. W. J.; Wang, N.; He, Q.; Chang, A.; Yang, C.-M.; Asakura, H.; Tanaka, T.; Hülsey, M. J.; Wang, C.-H.; Yu, J.; Yan, N. Zeolite-Encaged Pd–Mn Nanocatalysts for CO₂ Hydrogenation and Formic Acid Dehydrogenation. *Angew. Chem. Int. Ed.* **2020**, *59* (45), 20183–20191.
- (61) Jewell, L. L.; Davis, B. H. Review of absorption and adsorption in the hydrogen–palladium system. *Appl. Catal. A: Gen.* **2006**, *310*, 1–15.
- (62) Zhao, Z.; Huang, X.; Li, M.; Wang, G.; Lee, C.; Zhu, E.; Duan, X.; Huang, Y. Synthesis of Stable Shape-Controlled Catalytically Active β -Palladium Hydride. *J. Am. Chem. Soc.* **2015**, *137* (50), 15672–15675.
- (63) Bugaev, A. L.; Guda, A. A.; Lomachenko, K. A.; Srabionyan, V. V.; Bugaev, L. A.; Soldatov, A. V.; Lamberti, C.; Dmitriev, V. P.; van Bokhoven, J. A. Temperature- and Pressure-Dependent Hydrogen Concentration in Supported PdH_x Nanoparticles by Pd K-Edge X-ray Absorption Spectroscopy. *J. Phys. Chem. C* **2014**, *118* (19), 10416–10423.
- (64) Mager-Maury, C.; Bonnard, G.; Chizallet, C.; Sautet, P.; Raybaud, P. H₂-Induced Reconstruction of Supported Pt Clusters: Metal-Support Interaction versus Surface Hydride. *ChemCatChem* **2011**, *3* (1), 200–207.
- (65) Tew, M. W.; Miller, J. T.; van Bokhoven, J. A. Particle Size Effect of Hydride Formation and Surface Hydrogen Adsorption of Nanosized Palladium Catalysts: L 3 Edge vs K Edge X-ray Absorption Spectroscopy. *J. Phys. Chem. C* **2009**, *113* (34), 15140–15147.
- (66) Bard, A. J.; Faulkner, L. R. *Electrochemical Methods: Fundamentals and Applications, 2nd Edition*; Wiley, 2001.
- (67) Tauster, S. J.; Fung, S. C.; Garten, R. L. Strong metal-support interactions. Group 8 noble metals supported on titanium dioxide. *J. Am. Chem. Soc.* **1978**, *100* (1), 170–175.
- (68) Han, B.; Guo, Y.; Huang, Y.; Xi, W.; Xu, J.; Luo, J.; Qi, H.; Ren, Y.; Liu, X.; Qiao, B.; Zhang, T. Strong Metal–Support Interactions between Pt Single Atoms and TiO₂. *Angew. Chem. Int. Ed.* **2020**, *59* (29), 11824–11829.
- (69) Uchijima, T. SMSI effect in some reducible oxides including niobia. *Catal. Today* **1996**, *28* (1), 105–117.
- (70) Wu, C.; Cheng, D.; Wang, M.; Ma, D. Understanding and Application of Strong Metal–Support Interactions in Conversion of CO₂ to Methanol: A Review. *Energy & Fuels* **2021**, *35* (23), 19012–19023.
- (71) VandeVondele, J.; Krack, M.; Mohamed, F.; Parrinello, M.; Chassaing, T.; Hutter, J. Quickstep: Fast and accurate density functional calculations using a mixed Gaussian and plane waves approach. *Comput. Phys. Commun.* **2005**, *167* (2), 103–128.
- (72) Hutter, J.; Iannuzzi, M.; Schiffmann, F.; VandeVondele, J. cp2k: atomistic simulations of condensed matter systems. *Wiley Interdiscip. Rev. Comput. Mol. Sci.* **2014**, *4* (1), 15–25.

- (73) A. Heinecke; G. Henry; M. Hutchinson; H. Pabst. LIBXSMM: Accelerating Small Matrix Multiplications by Runtime Code Generation. In *SC '16: Proceedings of the International Conference for High Performance Computing, Networking, Storage and Analysis*, 2016; pp 981–991.
- (74) Marek, A.; Blum, V.; Johanni, R.; Havu, V.; Lang, B.; Auckenthaler, T.; Heinecke, A.; Bungartz, H.-J.; Lederer, H. The ELPA library: scalable parallel eigenvalue solutions for electronic structure theory and computational science. *J. Phys.: Condens. Matter* **2014**, *26* (21), 213201.
- (75) Borštnik, U.; VandeVondele, J.; Weber, V.; Hutter, J. Sparse matrix multiplication: The distributed block-compressed sparse row library. *Parallel Comput.* **2014**, *40* (5-6), 47–58.
- (76) Frigo, M.; Johnson, S. G. The Design and Implementation of FFTW3. *Proc. IEEE* **2005**, *93* (2), 216–231.
- (77) Kolafa, J. Time-reversible always stable predictor-corrector method for molecular dynamics of polarizable molecules. *J. Comput. Chem.* **2004**, *25* (3), 335–342.
- (78) Kühne, T. D.; Iannuzzi, M.; Del Ben, M.; Rybkin, V. V.; Seewald, P.; Stein, F.; Laino, T.; Khaliullin, R. Z.; Schütt, O.; Schiffmann, F.; Golze, D.; Wilhelm, J.; Chulkov, S.; Bani-Hashemian, M. H.; Weber, V.; Borštnik, U.; TAILLEFUMIER, M.; Jakobovits, A. S.; Lazzaro, A.; Pabst, H.; Müller, T.; Schade, R.; Guidon, M.; Andermatt, S.; Holmberg, N.; Schenter, G. K.; Hehn, A.; Bussy, A.; Belleflamme, F.; Tabacchi, G.; Glöß, A.; Lass, M.; Bethune, I.; Mundy, C. J.; Plessl, C.; Watkins, M.; VandeVondele, J.; Krack, M.; Hutter, J. CP2K: An electronic structure and molecular dynamics software package - Quickstep: Efficient and accurate electronic structure calculations. *J. Chem. Phys.* **2020**, *152* (19), 194103.
- (79) Perdew, J. P.; Burke, K.; Ernzerhof, M. Generalized gradient approximation made simple. *Phys. Rev. Lett.* **1996**, *77* (18), 3865.
- (80) Perdew, J. P.; Burke, K.; Ernzerhof, M. Generalized Gradient Approximation Made Simple. *Phys. Rev. Lett.* **1997**, *78* (7), 1396.
- (81) Gautier, S.; Steinmann, S. N.; Michel, C.; Fleurat-Lessard, P.; Sautet, P. Molecular adsorption at Pt(111). How accurate are DFT functionals? *Phys. Chem. Chem. Phys.* **2015**, *17* (43), 28921–28930.
- (82) Zhao, Y.; Truhlar, D. G. Benchmark databases for nonbonded interactions and their use to test density functional theory. *J. Chem. Theory Comput.* **2005**, *1* (3), 415–432.
- (83) Zhang, Y.; Yang, W. A Comment on the Letter by John P. Perdew, Kieron Burke, and Matthias Ernzerhof. *Phys. Rev. Lett.* **1998**, *80*, 890.
- (84) Grimme, S.; Antony, J.; Ehrlich, S.; Krieg, H. A consistent and accurate ab initio parametrization of density functional dispersion correction (DFT-D) for the 94 elements H-Pu. *J. Chem. Phys.* **2010**, *132* (15), 154104.
- (85) Grimme, S.; Ehrlich, S.; Goerigk, L. Effect of the damping function in dispersion corrected density functional theory. *J. Comput. Chem.* **2011**, *32* (7), 1456–1465.
- (86) VandeVondele, J.; Hutter, J. Gaussian basis sets for accurate calculations on molecular systems in gas and condensed phases. *J. Chem. Phys.* **2007**, *127* (11), 114105.
- (87) Lippert, G.; Hutter, J.; Parrinello, M. A hybrid Gaussian and plane wave density functional scheme. *Mol. Phys.* **1997**, *92* (3), 477–488.
- (88) Blöchl, P. E. Projector augmented-wave method. *Phys. Rev. B* **1994**, *50* (24), 17953–17979.
- (89) Kresse, G.; Joubert, D. From ultrasoft pseudopotentials to the projector augmented-wave method. *Phys. Rev. B* **1999**, *59* (3), 1758–1775.
- (90) Goedecker, S.; Teter, M.; Hutter, J. Separable dual-space Gaussian pseudopotentials. *Phys. Rev. B* **1996**, *54* (3), 1703–1710.
- (91) Hartwigsen, C.; Goedecker, S.; Hutter, J. Relativistic separable dual-space Gaussian pseudopotentials from H to Rn. *Phys. Rev. B* **1998**, *58* (7), 3641–3662.
- (92) Krack, M. Pseudopotentials for H to Kr optimized for gradient-corrected exchange-correlation functionals. *Theor. Chem. Acc.* **2005**, *114* (1), 145–152.
- (93) Kühne, T. D.; Krack, M.; Mohamed, F. R.; Parrinello, M. Efficient and accurate Car-Parrinello-like approach to Born-Oppenheimer molecular dynamics. *Phys. Rev. Lett.* **2007**, *98* (6), 66401.
- (94) Bussi, G.; Donadio, D.; Parrinello, M. Canonical sampling through velocity rescaling. *J. Chem. Phys.* **2007**, *126* (1), 14101.
- (95) Laio, A.; Rodriguez-Fortea, A.; Gervasio, F. L.; Ceccarelli, M.; Parrinello, M. Assessing the Accuracy of Metadynamics. *J. Phys. Chem. B* **2005**, *109* (14), 6714–6721.
- (96) Fiorin, G.; Klein, M. L.; Hénin, J. Using collective variables to drive molecular dynamics simulations. *Mol. Phys.* **2013**, *111* (22-23), 3345–3362.
- (97) Valsson, O.; Tiwary, P.; Parrinello, M. Enhancing Important Fluctuations: Rare Events and Metadynamics from a Conceptual Viewpoint. *Annu. Rev. Phys. Chem.* **2016**, *67* (1), 159–184.

- (98) consortium, T. P. Promoting transparency and reproducibility in enhanced molecular simulations. *Nat. Methods* **2019**, *16* (8), 670–673.
- (99) Tribello, G. A.; Bonomi, M.; Branduardi, D.; Camilloni, C.; Bussi, G. PLUMED 2: New feathers for an old bird. *Comput. Phys. Commun.* **2014**, *185* (2), 604–613.
- (100) Brehm, M.; Kirchner, B. TRAVIS - A Free Analyzer and Visualizer for Monte Carlo and Molecular Dynamics Trajectories. *J. Chem. Inf. Model.* **2011**, *51* (8), 2007–2023.
- (101) Brehm, M.; Thomas, M.; Gehrke, S.; Kirchner, B. TRAVIS — A free analyzer for trajectories from molecular simulation. *J. Chem. Phys.* **2020**, *152* (16), 164105.
- (102) Thomas, M.; Brehm, M.; Fligg, R.; Vöhringer, P.; Kirchner, B. Computing vibrational spectra from ab initio molecular dynamics. *Phys. Chem. Chem. Phys.* **2013**, *15* (18), 6608–6622.
- (103) Thomas, M.; Brehm, M.; Kirchner, B. Voronoi dipole moments for the simulation of bulk phase vibrational spectra. *Phys. Chem. Chem. Phys.* **2015**, *17* (5), 3207–3213.
- (104) Brehm, M.; Weber, H.; Thomas, M.; Hollóczki, O.; Kirchner, B. Domain Analysis in Nanostructured Liquids: A Post-Molecular Dynamics Study at the Example of Ionic Liquids. *ChemPhysChem* **2015**, *16* (15), 3271–3277.
- (105) Brehm, M.; Thomas, M. Optimized Atomic Partial Charges and Radii Defined by Radical Voronoi Tessellation of Bulk Phase Simulations. *Molecules* **2021**, *26* (7).
- (106) Brehm, M.; Thomas, M. An Efficient Lossless Compression Algorithm for Trajectories of Atom Positions and Volumetric Data. *J. Chem. Inf. Model.* **2018**, *58* (10), 2092–2107.
- (107) Rycroft, C. H. VORO++: a three-dimensional voronoi cell library in C++. *Chaos* **2009**, *19* (4), 41111.
- (108) Humphrey, W.; Dalke, A.; Schulten, K. VMD - Visual Molecular Dynamics. *J. Mol. Graph* **1996**, *14*, 33–38.
- (109) Stone, J. \em An Efficient Library for Parallel Ray Tracing and Animation, Computer Science Department, University of Missouri-Rolla, 1998.
- (110) Ravel, B.; Newville, M. ATHENA, ARTEMIS, HEPHAESTUS: data analysis for X-ray absorption spectroscopy using IFEFFIT. *J. Synchrotron. Radiat.* **2005**, *12* (Pt 4), 537–541.
- (111) Lomachenko, K. A.; Molokova, A. Y.; Atzori, C.; Mathon, O. Quantification of Adsorbates by X-ray Absorption Spectroscopy: Getting TGA-like Information for Free. *J. Phys. Chem. C* **2022**, *126* (11), 5175–5179.
- (112) Juan, A. de; Jaumot, J.; Tauler, R. Multivariate Curve Resolution (MCR). Solving the mixture analysis problem. *Anal. Methods* **2014**, *6* (14), 4964–4976.
- (113) Tauler, R.; Barceló, D. Multivariate curve resolution applied to liquid chromatography—diode array detection. *Trends Anal. Chem.* **1993**, *12* (8), 319–327.
- (114) Clark, A. H.; Nuguid, R. J. G.; Steiger, P.; Marberger, A.; Petrov, A. W.; Ferri, D.; Nachtegaal, M.; Kröcher, O. Selective Catalytic Reduction of NO with NH₃ on Cu–SSZ-13: Deciphering the Low and High-temperature Rate-limiting Steps by Transient XAS Experiments. *ChemCatChem* **2020**, *12* (5), 1429–1435.
- (115) Varandili, S. B.; Stoian, D.; Vavra, J.; Rossi, K.; Pankhurst, J. R.; Guntern, Y. T.; López, N.; Buonsanti, R. Elucidating the structure-dependent selectivity of CuZn towards methane and ethanol in CO₂ electroreduction using tailored Cu/ZnO precatalysts. *Chem. Sci.* **2021**, *12* (43), 14484–14493.
- (116) Clark, A. H.; Imbao, J.; Frahm, R.; Nachtegaal, M. ProQEXAFS: a highly optimized parallelized rapid processing software for QEXAFS data. *J. Synchrotron. Radiat.* **2020**, *27* (Pt 2), 551–557.

